Numerical Study on Self-Field Two-Dimensional Straight Anode MPD Thruster

Mahendhran M and Amit Kumar
Department of Aerospace Engineering, IIT Madras, Chennai, India

Abstract

A two-dimensional, compressible, finite volume, magnetohydrodynamic (MHD) solver for simulating inviscid and fully ionized plasma flow is developed to compute the flow field in Magnetoplasmadynamic (MPD) thrusters. Unsteady Euler's equations with body forces and Joule heating as momentum and energy sources are solved along with the solution of unsteady magnetic flux density equation derived from Maxwell's equation. The flow solver is validated against some benchmark gas dynamic problems. The MHD part of the solver is validated by computing a flared anode 2D MPD thruster flow. The effect of geometric configuration on the thruster performance is a studied by varying the length of cathode in a straight anode MPD thruster. A study on the effect of inlet mass flow rate is also performed for short (13 mm) and long (41 mm) cathode cases. The results are analyzed to understand the flow physics and to identify the configuration that yields better performance characteristics.

NOMENCLATURE

2D	Two-dimensional
Δx	Grid size in x-direction
ε_0	Permittivity of free space (=8.854 × 10^{-12} farad/m)
η_{thrust}	Thrust efficiency
μ_0	Magnetic permeability (=4π × 10^{-7} henry/m)
κ !	Boltzmann constant (= 1.38 × 10^{-23} J/K)
ρ	Density
ρ_e	Charge density
σ	Electrical conductivity
Ω	Volume of the cell
B	Self induced Magnetic field
$\mathbf{B}_0$	Self induced Magnetic field at inlet
c_p	Co-efficient of pressure
ds	Elemental surface area
e	Charge of electron (= 1.602 × 10^{-19} C)
e_t	Total specific energy of the fluid
E	Electric field
F	Thrust
$\mathbf{F_C}$	Convective fluxes
g_0	Gravitational acceleration on earth (9.81 m/s^2)
I	Inlet current
I_{sp}	Specific impulse
j	Current density
$\dot{m}$	Inlet Mass flow rate
n	Number density
n	Outward normal vector
p	Pressure
R	Specific gas constant

t	Unit tangent vector
T	Temperature
TPR	Thrust to Power Ratio
U	Conserved variables
v	Velocity vector (u, v components)
V	Potential difference
W	Width of the channel
x, *y*, *z*	Cartesian Coordinates

Subscripts

e	electrons
em	Eectromagnetic
x, y, z	Cartesian Coordinates

1. INTRODUCTION

Magnetoplasmadynamic thrusters are electromagnetic propulsion systems characterized by high thrust and high specific impulse among the other class of electric propulsion systems, making them one among the promising space propulsion systems for high thrust and long duration missions. The study of MPD thrusters has been done through various experimental, analytical and numerical models to understand and predict the essential features of the flow through discharge chamber of the MPD thrusters. Since MPD flows involve interactions of many complex phenomena like dissociation and ionization of the propellant gas into different species, formation of plasma, Joule/Ohmic heating and electromagnetic acceleration etc., developing an accurate numerical model becomes a cumbersome task. Thus simpler models that could capture the essential flow features of MPD thrusters are beneficial in providing some guidelines for preliminary design of these thrusters.

Several numerical models have been developed for MPD thrusters, which include an axisymmetric, one-fluid model by Kimura et al. [1], an idealized quasi-one-dimensional model by Kuriki et al. [2]. An axisymmetric, one fluid model was again developed by Yamada et al. [3] using finite difference technique and by Chanty and Martinez-Sanchez [4] using a finite volume method. A 2D, one fluid model was employed by Funaki et al. [5] and the results were compared with 2D MPD thruster experiments [6]. Funaki et al. [6] performed experiments on a multichannel 2D MPD arcjet operating in a quasi-steady mode, which was primarily used to visualize and correlate the flow field and the thruster performance of 2D MPD arcjets.

Recent works on MPD thrusters include an axisymmetric, self-field, viscous flow model with ionization non-equilibrium by Takeda and Yamamoto [7], where an LU-SGS implicit scheme is employed for the solution of Navier-Stokes equations. The model is used to compute the flow field of argon propelled MPD thruster with two levels of ionization. The results predicted are compared with experiments. Kubota et al. [8] employed a Lax-Friedrich explicit scheme for computing an axisymmetric, inviscid, partially ionized argon flow in a flared anode MPD thruster. Kubota et al. [9] also developed a viscous, ionization and thermal non-equilibrium model considering two levels of ionization for argon propellant. The effects of various geometric configurations were studied in induced and applied magnetic field cases. A finite volume solver with real gas equation of state and anomalous transport was employed by Sankaran et al. [10] to check for real gas effects in axisymmetric, argon propelled MPD thrusters. Miller and Martinez-Sanchez [11] studied the viscous and diffusive effects in argon propelled, self-field, non-equilibrium 2D MPD thrusters. Niewood and Martinez-Sanchez [12] modeled Hall effect and discussed its importance in a non-equilibrium 2D MPD model.

Many other models have been developed including two-fluid models that consider non-equilibrium ionization and dissociation reactions, thermal non-equilibrium between electrons and heavy species and turbulence into account for the numerical model [13]. These models could predict more details regarding the complex interactions of flow and the ionization processes but require considerable effort in developing a numerical code. The present work deals with a simple inviscid, two-dimensional, one fluid model which can predict the essential features of thrust generation in MPD thrusters. A finite volume method is employed for the spatial discretization and the unsteady governing equations are marched in time using a fourth order explicit Runge-Kutta method. The results obtained are validated against available numerical and experimental data of Ref. [5]. Finally, the effect of cathode length and inlet mass flow rate on the performance of straight anode MPD thruster is studied.

2. FORMULATION

2.1. Assumptions

The following assumptions are made in the numerical model developed for the simulation of MPD thruster:

1. Argon gas is used as the propellant. It is considered as fully ionized and quasi-neutral plasma as it enters the thrust chamber. Only single ionization is considered.
2. Plasma flow is two-dimensional (x-y plane) and the magnetic field acts only in the third dimension (z direction).
3. Plasma is considered to be inviscid and thermally non-conducting perfect gas. Complex processes like electrical sheath formation and radiation heat transfer are neglected.
4. Hall effect and the displacement current are neglected from Ohm's law and Ampere's law respectively.
5. Electrical conductivity of the plasma is taken as a scalar function of temperature and density, given by Spitzer-Harm's formulation.

2.2. Governing equations

The conservation equations governing unsteady, inviscid fluid flow are given by unsteady Euler's equation with the electromagnetic force and Joule heating terms included as source terms in the momentum and energy equations respectively.

Mass Conservation Equation:

$$\frac{\partial}{\partial t}\int_{\Omega}\rho d\Omega + \oint_{s}\rho\mathbf{v}\cdot\mathbf{n}ds = 0 \tag{1}$$

Momentum Equation:

$$\frac{\partial}{\partial t}\int_{\Omega}\rho\mathbf{v}d\Omega + \oint_{s}\rho\mathbf{v}\mathbf{v}\cdot\mathbf{n}ds = -\oint_{s}p\mathbf{n}ds + \int_{\Omega}\mathbf{j}\times\mathbf{B}d\Omega \tag{2}$$

Energy Equation:

$$\frac{\partial}{\partial t}\int_{\Omega}\rho e_t d\Omega + \oint_{s}(\rho e_t + p)\mathbf{v}\cdot\mathbf{n}ds = \int_{\Omega}\mathbf{j}\cdot\mathbf{E}d\Omega \tag{3}$$

Equation of State: $$p = \rho RT \tag{4}$$

Combining Maxwell's equation and Ohm's law, a single equation in terms of magnetic flux density is derived.

Maxwell's Equation:

- Ampere's law: $$\nabla\times\mathbf{B} = \mu_0\mathbf{j} \tag{5}$$
- Faraday's law: $$\nabla\times\mathbf{E} = -\frac{\partial\mathbf{B}}{\partial t} \tag{6}$$
- Gauss's law: $$\nabla\cdot\mathbf{E} = \frac{\rho_e}{\varepsilon_0} \tag{7}$$
- Law implying existence of magnetic dipoles

$$\nabla\cdot\mathbf{B} = 0 \tag{8}$$

Ohm's Law: $$\mathbf{j} = \sigma(\mathbf{E} + \mathbf{v}\times\mathbf{B}) \tag{9}$$

Since plasma is assumed quasi-neutral, the charge density ρ_e in eqn. (7) becomes zero and this equation becomes redundant in obtaining magnetic flux density equation.

Taking curl of eqn. (9) and substituting eqns. (5 and 6) leads to the magnetic field equation. Equation of Magnetic field/flux density:

$$\frac{\partial \mathbf{B}}{\partial t} - \nabla \times (\mathbf{v} \times \mathbf{B}) + \nabla \times \left(\frac{1}{\sigma \mu_0} \nabla \times \mathbf{B} \right) = 0 \tag{10}$$

Electrical conductivity for fully ionized plasma is given by Spitzer-Harm formulation [5]

$$\sigma = 1.5 \times 10^{-2} \frac{T^{3/2}}{\ln \Lambda} \tag{11}$$

Where Coulomb logarithm In Λ is

$$\ln \Lambda = \ln \left[\frac{12\sqrt{2}\pi\varepsilon_0^{3/2} (\kappa T)^{3/2}}{e^3 n_e^{1/2}} \right]$$

The integral form of two-dimensional governing equations are cast in vector form for easy numerical addressing, they are

$$\frac{\partial}{\partial t} \int_{\Omega} \mathbf{U} d\Omega + \oint_s \mathbf{F_c} \cdot \mathbf{n} ds = \int_{\Omega} \mathbf{Q} d\Omega \tag{12}$$

The vector of conserved variables is given by

$$\mathbf{U} = \begin{bmatrix} \rho \\ \rho u \\ \rho v \\ \rho e_t \end{bmatrix}$$

The vector of convective fluxes is given by

$$\mathbf{F_c} = \begin{bmatrix} \rho(\mathbf{v} \cdot \mathbf{n}) \\ \rho u(\mathbf{v} \cdot \mathbf{n}) + n_x p \\ \rho v(\mathbf{v} \cdot \mathbf{n}) + n_y p \\ (\rho e_t + p)(\mathbf{v} \cdot \mathbf{n}) \end{bmatrix}$$

The vector of volumetric source terms is given by

$$\mathbf{Q} = \begin{bmatrix} 0 \\ j_y B \\ -j_x B \\ j_x E_x + j_y E_y \end{bmatrix}$$

The magnetic flux density equation in two-dimensions with a component of **B** in z-direction is given by

$$\frac{\partial B_z}{\partial t} + \frac{\partial (u B_z)}{\partial x} + \frac{\partial (v B_z)}{\partial y} - \frac{\partial}{\partial x} \left(\frac{1}{\sigma \mu_0} \frac{\partial B_z}{\partial x} \right) - \frac{\partial}{\partial y} \left(\frac{1}{\sigma \mu_0} \frac{\partial B_z}{\partial y} \right) = 0 \tag{13}$$

3. NUMERICAL METHODOLOGY

The integral form of governing equations is discretized using a finite volume method. Finite-volume method is preferred because of its capability to handle complex geometries with reasonable accuracy and also since it uses integral form of equations for discretization. The resulting equations are in conservation form where fluxes are conserved, and hence the solution can accommodate flow discontinuities like shocks. There are two major kinds of finite-volume methods: cell-centered and cell-vertex methods, which differ by the storage of flow variables either in discrete cell volumes or at nodes, respectively. Both schemes are numerically similar and perform equally well on smooth grids. Cell centered schemes have an advantage of easier application of boundary conditions at domain boundaries but dual control volume cell-vertex method exhibits improved accuracy on distorted grids [14]. Considering the higher accuracy offered on distorted grids, the dual control volume cell-vertex method [14-17] is used in the present model.

3.1. Spatial discretization

A central or averaging scheme is used to obtain the convective fluxes at the faces of the control volume. Firstly, the fluxes at the vertices of the control volume are obtained by the averaging at the four nodes surrounding it and then these fluxes are transferred to the face centers by a two point averaging [16]. Thus six node points surrounding a control volume face contribute to the convective flux evaluation at a face center. The source term **Q**, which arises due to the terms, evaluated from the solution of the magnetic flux density equation is assumed constant over the control volume.

The final spatially discretized system of ordinary differential equations is given by

$$\frac{\partial}{\partial t}(\mathbf{U}\Omega)_{i,j} + \sum_{faces} \left(\mathbf{F}_{c,x} ds_x + \mathbf{F}_{c,y} ds_y\right)_{i,j} = (\mathbf{Q}\Omega)_{i.j} \tag{14}$$

3.2. Temporal discretization

The resulting system of ordinary differential equations in time is integrated using an explicit multistage method - The classical fourth order Runge-Kutta method. The preference for an explicit method is on the basis of its simplicity in implementation and the ease of extension of the solver for an increase in the number of equations. The explicit method also has an advantage of easily accommodating different schemes for the evaluation of convective fluxes, which would otherwise be difficult in case of implicit methods. The multistage method increases the stability of the explicit method in performing the numerical integration. The time step used for integration of discretized equations is obtained from a CFL criterion based method used for cell-vertex finite volume scheme by Crumpton et al. [18]. Global time stepping is adopted wherein the least time step of the whole domain is chosen for marching in time. This enables computation of any unsteady phenomenon, if it exists. Since the convective fluxes are obtained using an averaging scheme, which is generally unstable in convection-dominated flows; an artificial dissipation/viscosity is added to stabilize the numerical scheme. The method used here is the one proposed by Jameson et al. [19], which uses a combination of second and fourth order differences of the conserved variable based on a pressure based sensor which switches to a high second order dissipation at shock regions and to a low fourth order dissipation at smooth flow regions.

3.3. Discretization of the MHD equation

The two-dimensional magnetic flux density equation is taken in integral form and the convective fluxes are evaluated by central/averaging scheme as in the flow equations. The derivatives in the magnetic field equation are discretized using the application of divergence theorem where an auxiliary control volume is formed around each face of the cell, and the corresponding derivative is evaluated at cell face. The method allows for evaluation of gradients for arbitrary quadrilateral control volumes without high distortion [14,15].

3.4. Solution procedure

The time scale of the magnetic diffusion involved in the MHD equation is in the order of $\frac{\Delta x^2}{(1/\mu_0\sigma)}$, which is generally 2–3 orders less than the typical flow time scales involved [20]. Hence simultaneous solution of the flow and the magnetic field equation imposes severe restriction on the size of the time

step used. Therefore the magnetic induction equation is solved separately at each flow time step enabling a faster computation. The Magnetic induction equation is integrated in time by an implicit Euler method coupled with Alternating Direction Implicit (ADI) method using Thomas algorithm for solution of the resulting Tri-Diagonal Matrix (TDM) form of equations. This procedure allows the usage of larger time steps for the magnetic field equation further increasing the computation speed and numerical stability.

3.5. Boundary conditions

The boundary conditions for the numerical simulation are deduced from the physical flow parameters available from experiments.

3.5.1. Flow

A subsonic inlet is maintained by providing the inlet mass flow rate and the inlet gas temperature as physical boundary conditions. Density is extrapolated from the interior to maintain the numerical boundary condition. Since exit flow is accelerated to supersonic speeds all flow variables at the exit are extrapolated from the interior. The electrode and insulator surfaces are treated as slip walls, where only tangential component of velocity is allowed, ensuring tangential slip with a zero normal component of velocity and zero normal pressure gradient, ensuring no flow across the walls. The walls are also treated as adiabatic. The axis is maintained as a symmetry boundary with zero gradients of pressure, temperature, axial velocity and zero normal velocity across it.

3.5.2. Electromagnetic

To simulate the discharge due to the electric potential across the electrodes, the amount of input current is specified in terms of magnetic field at the inlet, which is given by

$$B_0 = \frac{\mu_0 I}{2W}, \tag{15}$$

The electrodes represent equipotential surfaces and to maintain them at a constant potential the electric field must be acting normal to the electrode surfaces. Hence the tangential component of electric field is made zero, which ensures equipotential condition at the electrodes. The magnetic field at the axis and outlet are maintained as zero implying that the magnetic field does not cross these boundaries.

The convergence of the numerical solution is monitored using L2 norm in computing the scaled residuals of continuity, x and y-momentum and energy equations. The residual of the magnetic field equation is also monitored separately at each flow time step. The solution after the least possible and unaltered value of residual is taken as the final converged solution.

3.6. Evaluation of performance parameters

The following performance parameters are computed based on the resulting flow field to assess the overall performance of the MPD thrusters.

The total thrust produced is the sum of momentum and pressure thrust components, which is computed by the expression

$$F_{total} = F_{momentum} + F_{pressure} = \int_{exit} \rho u^2 dy + (p_{exit} - p_{ambient}) A_{exit} \tag{16}$$

The exit of the MPD thruster is assumed to be at vacuum and hence $P_{ambient} = 0$ Pa is used.

The specific impulse,

$$I_{sp} = \frac{F_{total}}{\dot{m} g_0} \tag{17}$$

The Electromagnetic forces are computed as

$$F_{em,x} = \int_{\Omega} j_y B_z d\Omega \tag{18}$$

$$F_{em,y} = \int_{\Omega} -j_x B_z d\Omega \tag{19}$$

The Joule Heating is computed as

$$Joule\,Heating = \int_{\Omega} \mathbf{j} \cdot \mathbf{E} d\Omega \tag{20}$$

The input potential difference is computed as the average potential difference across the electrodes and is given by

$$V = -\int_{anode}^{cathode} \mathbf{E} \cdot \mathbf{t} d\mathbf{s} \tag{21}$$

The Input Power is computed as

$$Input\,Power = V \cdot I \tag{22}$$

A potential difference of 20 V is added to the computed potential difference to account for the potential drop due the electrical sheath formation near the electrode walls [14].

The Thrust to Power Ratio (TPR) computed as a measure of thrust produced per *kW* of electrical energy expended,

$$TPR = \frac{F_{total}}{Input\,Power} \tag{23}$$

The thrust efficiency (η_{thrust}), which is the measure of the fraction of input power converted to kinetic power, is given by [9]

$$\eta_{thrust} = \frac{\left(F_{total} - F_{in}\right)^2}{2\dot{m} \times Input\,Power} \tag{24}$$

F_{inlet} is the inlet momentum flux,

$$F_{in} = \dot{m}\bar{u}_{inlet} \tag{25}$$

Where $\bar{U}_{inlet}$ denotes the average axial velocity at inlet.

4. DISCUSSION OF RESULTS

The flow solver developed is validated by computing numerical solutions for some benchmark gas dynamic problems, which include flow over a compression-expansion corner, flow through a convergent-divergent nozzle, where, in both cases the results are compared with available analytical results. The flow over a circular arc airfoil is also computed and the results are compared with available experimental [21] and numerical [22] data.

The MHD numerical code developed is validated against the numerical and experimental results of 2D flared anode MPD thruster. Then, the computations are used to study the performance of straight anode MPD thruster.

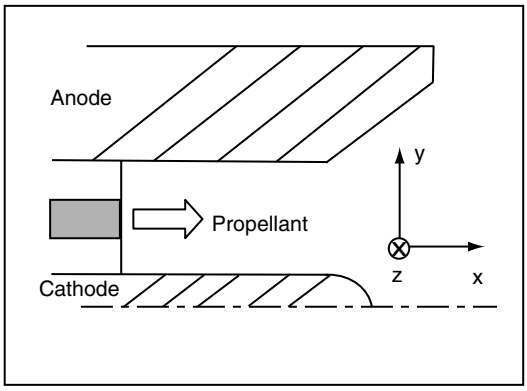

Figure 1. Schematic cross sectional view of an MPD Thruster.

4.1. Validation of the MHD solver: flared anode MPD thruster flow

To validate the MHD solver developed, flow through a self-field MPD thruster is simulated. The 2D MPD thruster chosen is a simplified form of the experimental model chosen by Funaki et al. [5]. A schematic diagram of the thruster used is shown in fig. 1. The flow conditions correspond to an inlet mass flow rate of 2.5 g/s and a discharge current of 8 kA. Different grid sizes are used to check for the independence of results due to the grids chosen. Figure. 2 shows the plot of computational domain and various flow field parameters in the domain. The thrust shown in fig. 2 (e & f) corresponds to the momentum thrust at exit.

The current contours (which are similar as the induced magnetic field contours, since the induced magnetic field and current are directly proportional) in fig. 2 (c) indicate that a concentration of current lines near the cathode tip which is due to the geometric orientation, a sharp corner and a shorter length of cathode compared to the anode. This higher current concentration near the cathode surface creates a higher Lorentz force and Joule heating giving rise to higher flow acceleration in this region, which can be seen from the plots of velocity vectors and axial velocity along a horizontal line midway through the flow domain shown in fig. 2 (d). The temperature contour in fig. 2 (c) indicates some regions with very high and unrealistic temperatures (> 20,000 K) in the flow field, whereas the experimental temperatures measured were around 15,000-18,000 K.

This should be attributed to the assumption that the plasma entering the thrust chamber is completely singly ionized which means that there are no ionization- recombination reactions to absorb the energy release due to the Joule heating and hence reduce the plasma temperatures. Considering ionization-recombination reactions could reduce these very high temperatures to realistic values. The performance characteristics that we are interested get very less affected by these small regions of high temperatures and hence the model could be employed for the present purposes. The scaled residuals of the numerical solution converged to values of order 10^{-15} in 15,000 iterations. A 51×31 grid size was chosen for the comparison of the present numerical results with that of Funaki et al. [5]. Figure. 2 (e) indicates that the total band of variation in the thrust computed for solution on different grids is around 4.6 %. Hence 51×31 grid is sufficient for capturing the major flow features and for further computations, 51×31 grid points are employed.

The variation of thrust with discharge current is shown in fig. 2 (f), which gives a plot of exit momentum thrust versus discharge current over the range of 1-16 kA. The plot also shows numerical [5] and experimental [6] results of Funaki et al. in the 8-14 kA current region for comparison, which indicate good agreement with experimental results with a deviation at high current levels but show only a qualitative agreement with the numerical results. The reason could be due to the difference in evaluation of momentum thrust. In Ref. [5], the momentum thrust is taken as the product of mass flow rate and the average axial exit velocity whereas an integral of momentum flux over all the cell faces at exit is computed in the present simulation. The mismatch between the computational results shown in fig. 2 (d) could have been caused as a result of arbitrary grid density employed and the difference in computational techniques used. Funaki et al. [5] employed a generalized coordinate finite difference technique with a TVD-Mac Cormack scheme and Roe's dissipation for the discretization of convective fluxes, whereas a finite-volume central/averaging technique with Jameson's artificial dissipation is used in the present model.

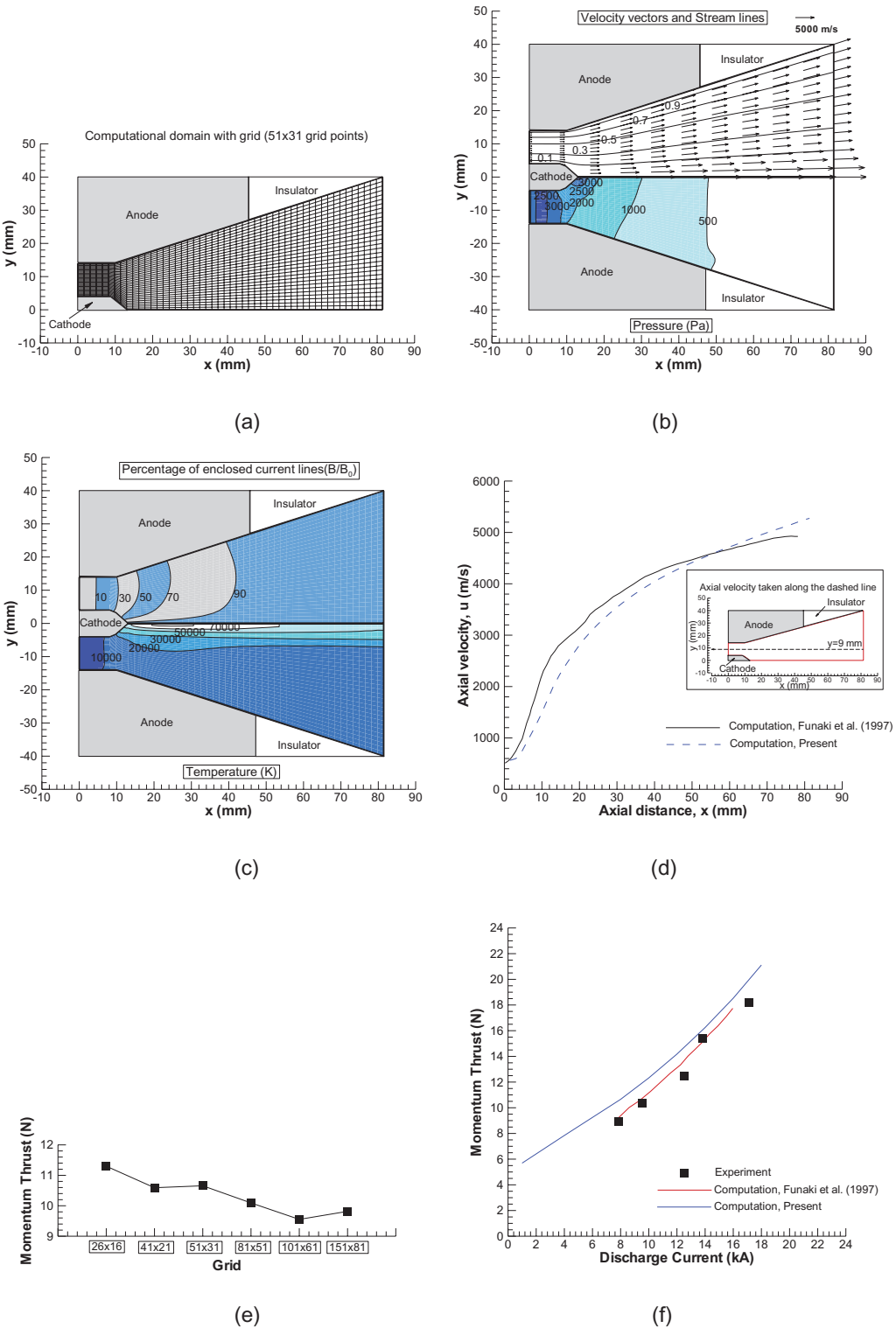

Figure 2. Various plots for flared anode MPD thruster – (a) Computational domain and the grid (b) Velocity vectors, Stream lines and Pressure contours (c) Magnetic field and Temperature contours (d) Axial velocity along a horizontal line drawn from inlet to exit, at y=9 mm (shown as inset) (e) Momentum thrust on different grids (f) Momentum thrust as a function of discharge current.

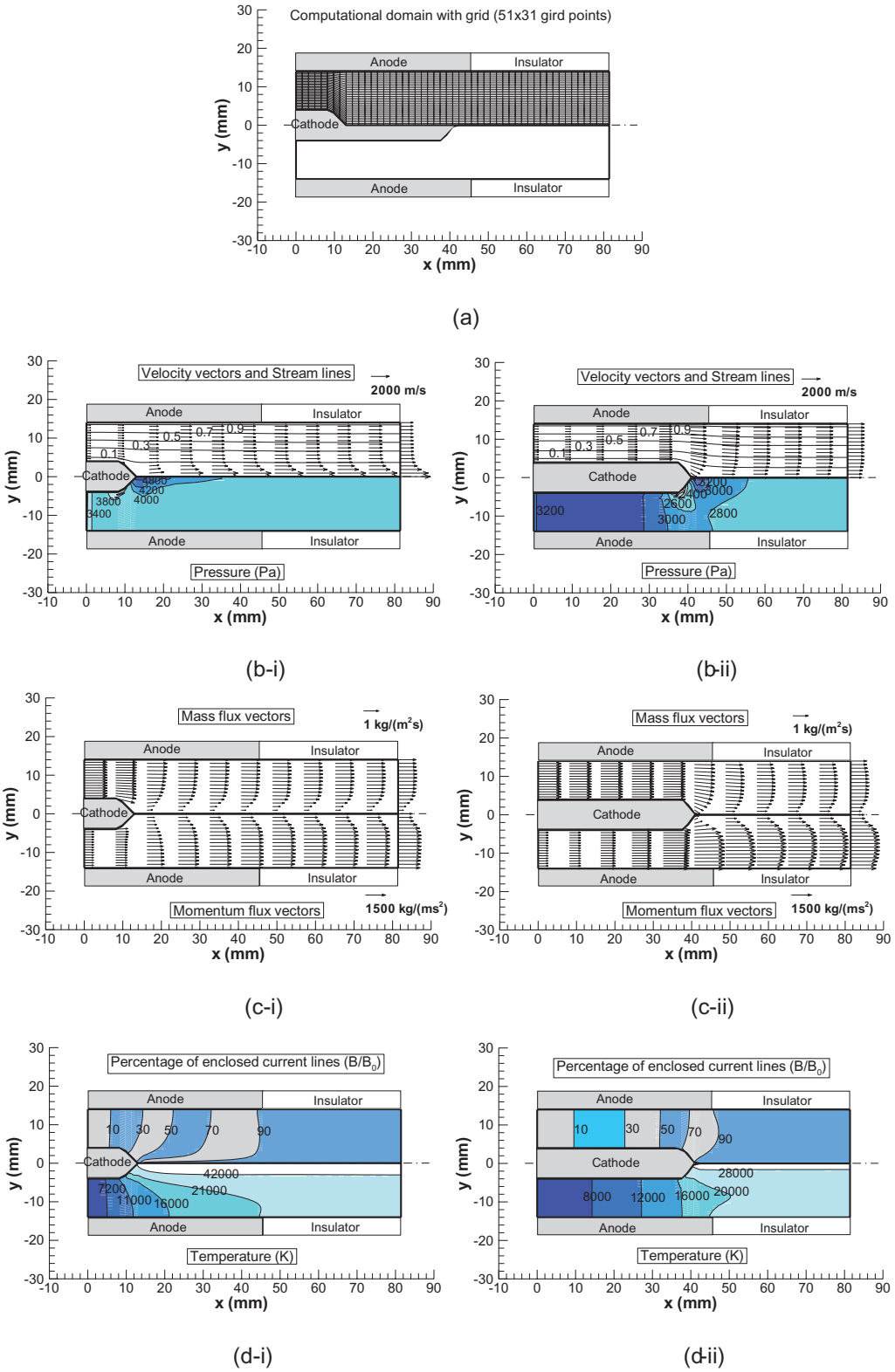

Figure 3. Plots of flow field variables for short (referred as i) and long (referred as ii) cathode cases – (a) Domain and the grid (b) Stream lines along with Velocity vectors and pressure contours (c) Mass flux and Momentum flux vectors (d) Normalized Magnetic field and Temperature contours

4.2. Straight anode MPD thruster flow

The straight anode MPD thruster is numerically modeled and studied to understand the effects of variation in the electrode configuration. A straight outer anode is used, which does not possess any area variation effects as flared and convergent-divergent nozzle anode MPD thrusters, which enables us to study the electromagnetic effects on the gas dynamic flow separately.

The study involves fixing the anode length (49.464 mm) and varying the cathode length. Two configurations with cathode lengths of 13 mm and 41 mm, chosen as the short and long cathode cases are considered for the study. The lengths chosen correspond to the experimental values used by Funaki et al. [6]. The domain and the grids for the short and long cathode cases are shown in fig. 3 (a). 51?31 grid points are used in both the cases. The boundary conditions that correspond to a mass flow rate of 2.5 g/s and discharge current of 8 kA are applied.

The computational domain for both the cases is shown in fig. 3 (a) and the resulting flow field parameters are shown in fig. 3 (b-d).

Table.1 lists some performance parameters for a comparison between the short and long cathode cases. The major difference in flow characteristics between the short and long cathode cases arises due to the difference in surface area of the cathode which leads to an increased current concentration for smaller cathode surface. This can be seen from the induced magnetic field lines in the flow field plots (fig. 3 (d)). This induced magnetic field along with the current density and electric field gives rise to Lorentz force and Joule heating respectively. Hence the short cathode case experiences higher Lorentz force and Joule heating, leading to slightly higher electromagnetic thrust compared to long cathode. The higher heating also increases the thermal energy input, where the heated plasma expands to produce a higher momentum thrust. The increase in the pressure thrust for short cathode is due to the smaller pressure drop in the shorter length before the cathode tip, whereas in the long cathode case there is gradual heating along the length of the cathode causing a larger pressure drop.

4.2.1. A study on the effect of cathode length variation

As a further investigation regarding the cathode length, a study by increasing cathode lengths from 5-55 mm in an interval of 5 mm is performed and various performance parameters obtained are plotted in fig. 4. It can be observed that the total thrust decreases with increase in cathode length. The momentum thrust component increases and the pressure component decreases with cathode length, this trend reverses at 45-55 mm length, which is due the higher drop in average exit velocity and slight increase in average exit temperature. This indicates that major part of energy is wasted as thermal energy instead of being converted into kinetic energy in this cathode length region. This can also be observed from the plot of thrust efficiency, which shows a decreasing trend with increasing length.

Table 1. Comparison of some performance parameters for long and short cathode cases

Parameters	Short cathode	Long cathode
$U_{average,exit}$	1716.308	1759.452
$T_{average,exit}$	45 866.290	22 806.455
$F_{electromagnetic,\ x}$	2.787	2.434
$F_{electromagnetic,y}$	–1.540	–0.108
Total Joule heating	33.764	23.082
$F_{momentum}$	3.679	4.428
$F_{pressure}$	9.167	6.530
F_{total}	12.846	10.958
I_{sp}	550.534	447.946

Nomenclature (units): u- axial velocity (m/s), T- Temperature (K), F- Force/ Thrust (N), Total Joule Heating (kW) and I_{sp} -Specific Impulse (s)

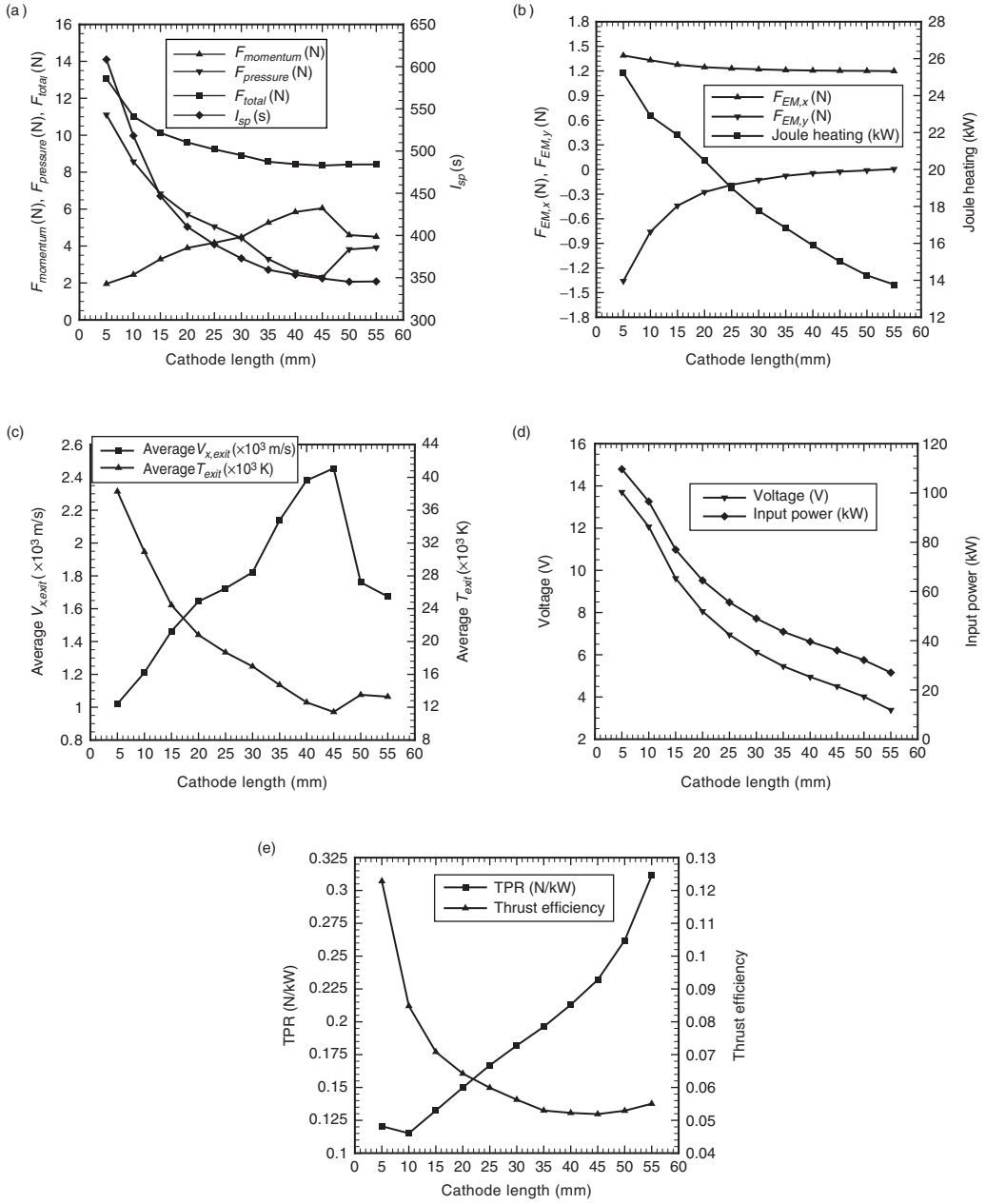

Figure 4. Plot of various performance parameters as a function of cathode length - (a) Different components of thrust and specific impulse (b) Electromagnetic forces and Joule heating (c) Average axial velocity and average temperature at exit (d) Average electrode potential difference and input power (e) Thrust to power ratio and thrust efficiency

Since the power input decreases with increase in cathode length due to lesser current concentration at cathode, the TPR increases with length indicating a requirement of low power and hence less weight of the power plant system for the thrust produced.

4.2.2. A study on the effect of inlet mass flow rate variation

To check the performance of the straight anode MPD thruster operating at various I_{sp} regions, the inlet mass flow rate is decreased from 2.5 g/s to 0.5 g/s in 0.5 g/s interval. The simulations are carried out for short cathode (13 mm) and long cathode (41 mm) cases to check for the effect of mass flow rate on both the cases. The variation in performance parameters obtained for the short and long cathode cases are plotted in fig. 5

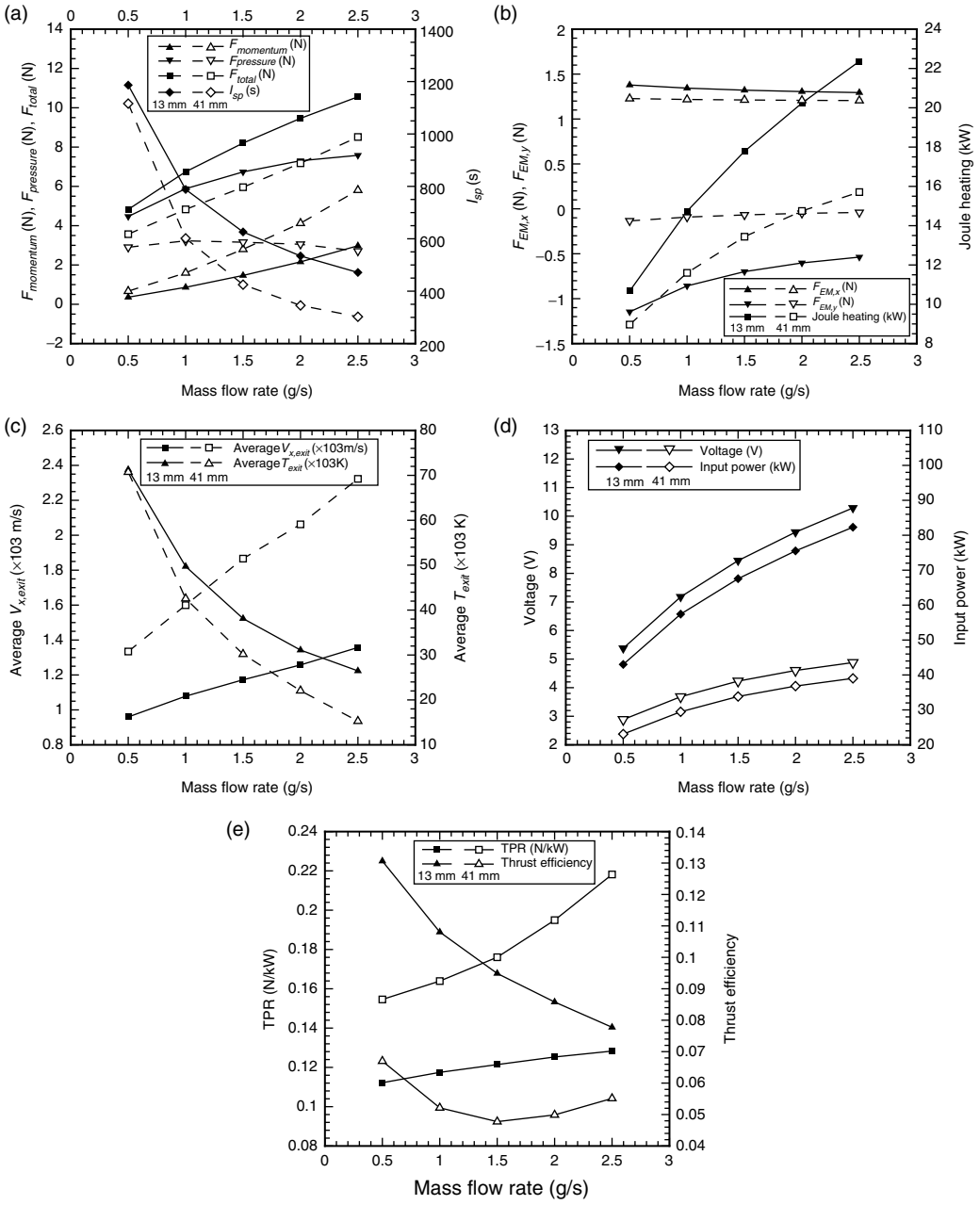

Figure 5. Plot of various performance parameters as a function of mass flow rate for short cathode (13 mm) and long cathode (41 mm) cases - (a) Different components of thrust and specific impulse (b) Electromagnetic forces and Joule heating (c) Average axial velocity and average temperature at exit (d) Average electrode potential difference and input power (e) Thrust to power ratio and thrust efficiency

The plots indicate that at low mass flow rates the short cathode case produce higher thrust and I_{sp} compared to the long cathode case. The electromagnetic component of thrust slightly decreases with increase in mass flow rate. The input power remains high for the short cathode case at smaller mass flow rates. The Joule heating increases with increase in mass flow rate since the energy input per unit time is absorbed more readily by the high mass flow rate in a unit time. There is a steep increase in input power for short cathode case compared to long cathode case. Since higher mass flow rates can accommodate more energy, the exit temperatures are less for high mass flow rate cases. The average

exit velocities increase with mass flow rate, for both short and long cathode cases. The decrease in exit temperature and the increase in exit velocity (with an increase mass flow rate) are steeper for short cathode case compared to long cathode case.

The thrust efficiency is high at low mass flow rates and high I_{sp} region for both short and long cathode cases. The thrust efficiency of the short cathode case exhibits a monotonically decreasing trend whereas in long cathode case there is a decrease till a mass flow rate of 1.5 g/s and an increase thereafter, caused by the higher increase in thrust and a moderate increase in input power at this mass flow rate regions. The TPR increases with mass flow rate for both short and long cathode cases with a steep increase for the long cathode case.

5. CONCLUSIONS

The numerical model developed was employed to study effects of cathode length and inlet mas: flow rate for the Straight Anode MPD thruster. Some major conclusions that could be drawn basec on the results are summarized as:

- The cathode surface area (which is directly proportional to the length of the cathode) decides the magnitude of current density and electric field, which in turn produce Lorentz body force on charged particles and Joule heating. Even though MPD thrusters operate at high current levels (of the order of several kilo Amperes), the major part of momentum thrust results from the thermal expansion of heated plasma, the contribution of electromagnetic thrust component remains low (say about 20 %).
- The longer cathode configuration is better in terms of thrust to power ratio (but at lower specific impulse). This is mainly due to the low power consumption at same current level compared to shorter cathode configuration. The thrust to power ratio also increases with mass flow rate. In terms of thrust efficiency the shorter cathodes are better. Further there is increase in efficiency at lower mass flow rates. Since the change in vehicle velocity (delta V) is the major concern in rocket performance, the benefit from higher specific impulse (or equivalent exhaust velocity) dominates over that from system (power plant) weight reduction. Therefore the thruster design would primarily be dictated by thrust efficiency. Hence short cathode MPD thrusters would be a choice over the long cathode thrusters.
- In straight anode MPD thruster, the short cathode thruster produces high thrust and high specific impulse compared to the long cathode thruster. This is due to the higher pressure thrust component due to flow under-expansion in the inter-electrode region. Therefore, the use of flared or convergent-divergent anode MPD thrusters would provide further expansion of plasma in the region aft of the inter-electrode region resulting in higher momentum thrust and total thrust compared to straight anode MPD thrusters.

REFERENCES

[1] Kimura, I., Toki, K., and Tanaka, M., Current Distribution on the Electrodes of MPD Arcjets, *AIAA Journal*, 1982, 20(7), 889-892.

[2] Kuriki, K., Kunii, Y., and Shimizu, Y., Idealized Model for Plasma Acceleration in an MHD Channel, *AIAA Journal*, 1983, 21(3), 322-326.

[3] Yamada H., Ao T., and Fujiwara, T., Two-dimensional Analysis of a Flow in an MPD Thruster, *Report SP No.3, JAXA*, 1985, 67-76.

[4] Chanty, J. M. G., and Martinez-Sanchez, M., Two-dimensional Numerical Simulation of MPD Flows, *AIAA-87-1090*, *In: AIAA/DGLR/JSASS 19th International Electric Propulsion Conference,* Colorado Springs, Colorado, 1987.

[5] Funaki, I., Toki, K., and Kuriki, K., Numerical Analysis of a Two-Dimensional Magnetoplasmadynamic Arcjet, *Journal of Propusion and Power*, 1997, 13(6), 789-795.

[6] Funaki, I., Toki, K., and Kuriki, K., Electrode Configuration Effect on the Performance of a Two-Dimensional Magnetoplamadynamic Arcjet, *Journal of Propulsion and Power*, 1998, 14(6), 1043-1048.

[7] Takeda, H., and Yamamoto, S., Implicit Time-Marching Solution of Partially Ionized Flows in Self-Field MPD Thruster, *Trans. Japan Soc. Aero. Space Sci*., 2002, 44(140), 223-228.

[8] Kubota, K., Funaki, I., and Okuno, Y., Numerical Simulation of a Self-field MPD Thruster using Lax- Friedrich Scheme, *Proceedings of ISSS-7*, 2005.

[9] Kubota, K., Funaki, I., and Okuno, Y., Numerical Study of Electrode Geometry Effects on Flow field in Two-Dimensional MPD Thrusters, *IEPC-2007-87*, *In: 30th International Electric Propulsion Conference*, Florence, Italy, 2007.

[10] Sankaran, E., Choueiri, E. Y., and Jardin, S. C., Application of New Numerical Solver to the Simulation of MPD flows, *AIAA-2000-3537*, 2000.

[11] Miller, S., and Martinez-Sanchez, M., Viscous and Diffusive Effects in MPD flows, *AIAA-90-2606*, *In: AIAA/DGLR/JSASS 21th International Electric Propulsion Conference,* Orlando, Florida, 1990.

[12] Niewood, E. H., and Martinez-Sanchez, M., A Two Dimensional Model of an MPD Thruster, *AIAA-91-2344*, *In: AIAA/DGLR/JSASS 27th International Electric Propulsion Conference,* Sacramento, California, 1991.

[13] Heiermann, J., and Auweter-Kurtz, M., Numerical and Experimental Investigation of the Current Distribution in Self-Field Magnetoplasmadynamic Thrusters, *Journal of Propulsion and Power*, 2005, 21(1), 119-128.

[14] Blazek, J., *Computational Fluid Dynamics: Principles and Applications*, Elsevier, 2001.

[15] Fletcher, C. A. J., *Computational Techniques for Fluid Dynamics - Vol. 1*, Springer-Verlag, 1988.

[16] Hirsch, C., *Numerical Computation of Internal and External Flows- Vol. 1*., John Wiley and sons, 1988.

[17] Hall, M. G., A Vertex-Centroid Scheme for Improved Finite-Volume Solution of the Navier-Stokes Equations, *AIAA-91-1540*, 1991.

[18] Crumpton, P. I., Mackenzie, J. A., and Morton K. W., Cell Vertex Algorithms for the Compressible Navier-Stokes Equations, *Journal of Computational Physics*, 1993, 109, 1-15.

[19] Jameson, A., Schmidt, W., and Turkel, E., Numerical Solution of Euler Equations by Finite Volume Methods Using Runge Kutta Time Stepping Schemes, *AIAA Paper 81-1259*, 1981.

[20] Niewood, E. H., *Transient One Dimensional Numerical Simulation of Magnetoplasmadynamic Thrusters*, *M.S Thesis*, Massachusetts Institute of Technology, Cambridge, MA, 1989.

[21] Knechtel, E. D., Experimental Investigation At Transonic Speeds of Pressure Distributions over Wedge and Circular-arc Airfoil Sections and Evaluation of Perforated-Wall Interference, *NASA TN-D-15*, 1959.

[22] Madhavan, N. S., and Swaminathan, V., Implicit Numerical Solution of Unsteady Euler Equations for Transonic Flows, *Indian Journal of pure and applied mathematics*, 1986, 17(9), 1164-1173.